Tectonophysics 590 (2013) 189–195

Contents lists available at SciVerse ScienceDirect

Tectonophysics

journal homepage: www.elsevier.com/locate/tecto

# High-resolution fault image from accurate locations and focal mechanisms of the 2008 swarm earthquakes in West Bohemia, Czech Republic

Václav Vavryčuk *, Fateh Bouchaala, Tomáš Fischer

*Institute of Geophysics, Academy of Sciences, Boční II/1401, Praha 4, Czech Republic*

ARTICLE INFO

*Article history:*
Received 26 July 2012
Received in revised form 23 January 2013
Accepted 27 January 2013
Available online 4 February 2013

*Keywords:*
Earthquake location
Failure criterion
Fault friction
Focal mechanism
Tectonic stress

ABSTRACT

We have analyzed 463 micro-earthquakes in the magnitude range from 0.5 to 3.8 that occurred during the 2008 earthquake swarm in West Bohemia, Czech Republic, in order to screen the detailed structure of the focal zone situated at depths between 7 and 11 km. The double-difference location method was applied to records of 22 local seismic stations with an epicentral distance of less than 25 km in order to retrieve highly accurate locations of hypocenters with an accuracy of less than 20 m. The hypocenters are well-clustered and distinctly map the system of activated faults. The fault system has a complex geometry being composed of several fault segments with different orientations. Some of the segments intersect each other. The orientations of the segments coincide well with the focal mechanisms. We have introduced and evaluated the so-called fault instability of the individual fault segments. The fault instability ranges from 0 (most stable faults) to 1 (most unstable faults) and measures the susceptibility of the fault to be activated under specified stress. In the West Bohemia focal zone, two fault segments are optimally oriented with respect to the tectonic stress being characterized by an instability value higher than 0.9. Tractions on these fault segments are concentrated in the Mohr's diagram in the area of validity of the Mohr–Coulomb failure criterion and the associated micro-earthquakes are mainly shear. The other fault segments are slightly misoriented with instability values between 0.7 and 0.9, and the shear traction is significantly lower. These earthquakes are probably more tensile and activated most likely by the local redistribution of Coulomb stress during swarm activity.



## 1. Introduction

The West Bohemia/Vogtland region is the border area between the Czech Republic and Germany (Fig. 1) and the most seismically active region in the Bohemian Massif (Babuška et al., 2007). Active tectonics in this geothermal area is expressed by the presence of Tertiary or Quaternary volcanism, mineral springs, emanations of $CO_2$, and by pertinent seismic activity in the form of earthquake swarms. The most prominent earthquake swarms occurred recently in 1985/86, 1997, 2000 and in 2008 in the same epicentral area called the Nový Kostel zone (e.g., Fischer and Horálek, 2003; Fischer et al., 2010; Vavryčuk, 2002, 2011a, 2011b). Their duration was from 2 weeks to 2 months and the activity was located typically at depths ranging from 7 to 12 km.

One of the strongest earthquake swarms occurred in October 2008 (Fischer et al., 2010). This swarm lasted for about four weeks and involved more than 25,000 micro-earthquakes with magnitudes higher than −0.5. The magnitude of the strongest earthquake reached 3.8. The hypocenters were located at depths of 7.5–11 km. The micro-earthquakes were recorded by 22 three-component short-period West Bohemia Network (WEBNET) stations installed in the area and surrounding the swarm epicenters with epicentral distances of less than 25 km (Fig. 1). The sampling frequency of the velocity records was 250 Hz, the frequency response being flat at least between 1 and 60 Hz. The configuration of the network guarantees high-quality recording and a good focal sphere coverage of the studied earthquakes.

The tectonic structure of the area is characterized by two main fault systems well expressed on the surface: the Sudeten NW–SE fault system and the Eger–Rift WSW–ENE fault system. The NW–SE fault is probably a continuation of the Mariánské Lázně fault (see Fig. 1). The recently active fault systems are, however, different. The most active is the left-lateral strike-slip fault running N–S with a strike of N169°E. During some periods, the seismicity is associated also with the right-lateral strike-slip fault in the WNW direction with a strike of N304°E (Bankwitz et al., 2003; Vavryčuk, 2011a). The maximum compressive stress, determined through an inversion of focal mechanisms, has an azimuth of N146°E (Vavryčuk, 2011a). This direction is close to the average direction of N144°E of the maximum compression in Western Europe (Heidbach et al., 2008).

* Corresponding author. Tel: +420267103020.
*E-mail address:* vv@ig.cas.cz (V. Vavryčuk).

0040-1951/$ – see front matter © 2013 Elsevier B.V. All rights reserved.
http://dx.doi.org/10.1016/j.tecto.2013.01.025

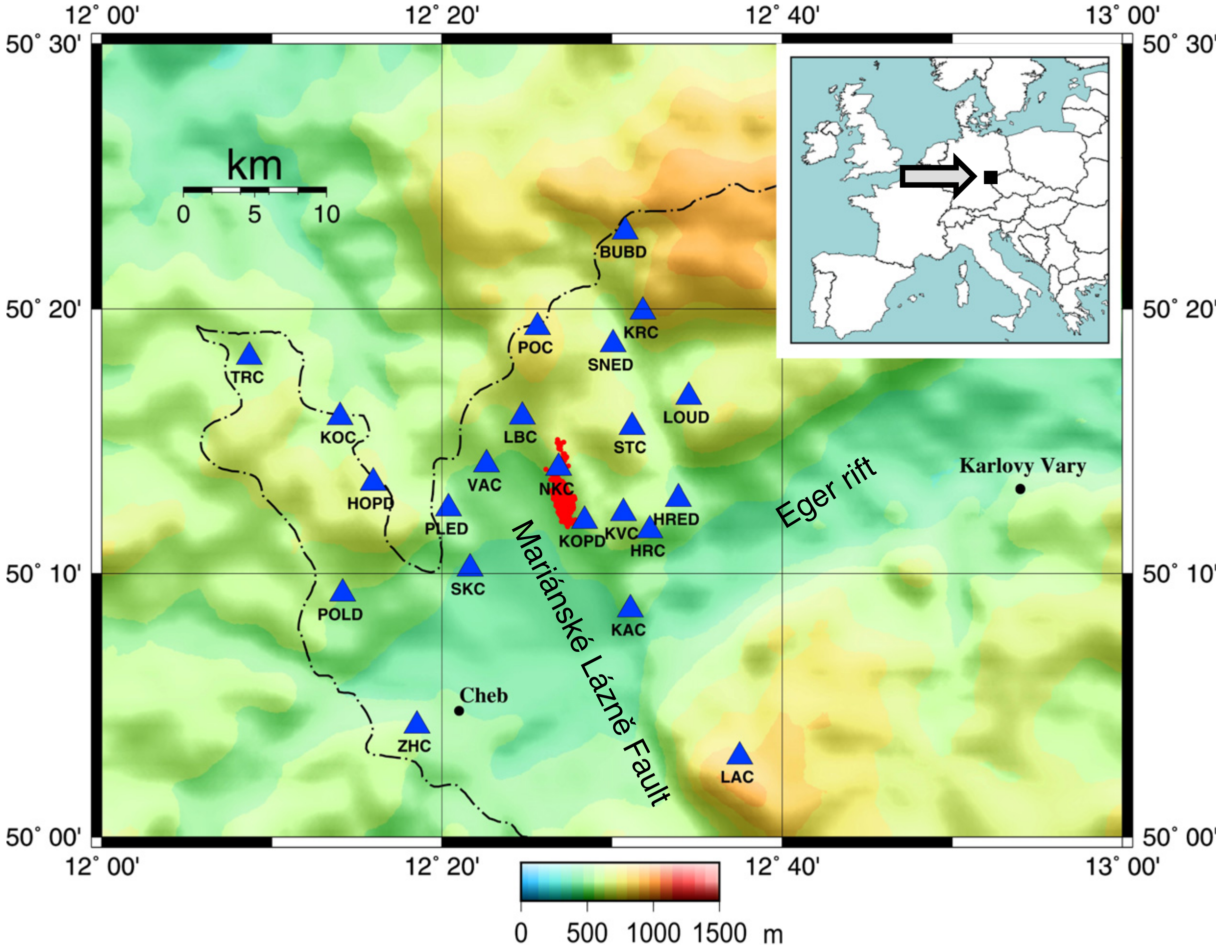


**Fig. 1.** Topographic map of the West Bohemia/Vogtland region. The epicenters of the 2008 swarm earthquakes are marked by red dots. The WEBNET stations are marked by blue triangles. The dashed-dotted line shows the border between the Czech Republic and Germany.

Interestingly, the $\sigma_3$ axis is horizontal, but the $\sigma_1$ and $\sigma_2$ axes are inclined by about 45° (Vavryčuk, 2011a).

## 2. Locations and focal mechanisms

### *2.1. Double-difference locations*

We located 463 microearthquakes of the 2008 West Bohemia earthquake swarm recorded at all WEBNET stations in order to depict the detailed structure of the focal zone. The initial locations were calculated by the FASTHYPO code (Hermann, 1979) in a layered velocity model (see Table 1) obtained by refining the model of Málek et al. (2000) and using the P and S arrival times. The location accuracy is affected mostly by two factors: first, by uncertainties in the velocity model, and second, by errors in picking the arrival times. By minimizing the effects of these errors, the location accuracy can be significantly increased and the fault imaging improved. To do this, we apply the double-difference relocation method of Waldhauser and Ellsworth (2000). Based on the initial hypocenter locations, we use hypocenter pairs with a separation of less than 0.7 km. Each hypocenter had to be connected to a minimum of 10 other neighbors. The catalog of differential times is calculated from manually picked P and S wave arrivals, respectively. Additionally, we use the cross-correlation differential times computed in the band-pass from 3 to 10 Hz. We considered only data with a normalized correlation coefficient higher than 0.8. The same P-wave velocity model as for the initial locations (Table 1) was used for relocations and the same ratio between the P and S wave velocities, Vp/Vs = 1.70, was retained. The relative accuracy of the foci within the foci cluster is estimated to be less than 20 m (Bouchaala et al., 2013). This value was obtained by repeating the locations of arrival times perturbed by random errors of up to ±4 ms for the P waves and of up to ±8 ms for the S waves. The high relative precision of the locations was achieved because: (1) an extensive data set of micro-earthquakes observed at many local seismic stations was located, (2) the foci are concentrated in a small focal zone and they allow for creating a large number of foci pairs, and (3) the cross-correlation differential times are determined with a high accuracy. The absolute position of the cluster is about 100 m in the horizontal plane and 350 m in depth being mainly affected

**Table 1**
The West Bohemia velocity model.

| Layer number | Depth (km) | P-wave velocity (km/s) |
|---|---|---|
| 1 | 0.0 | 4.30 |
| 2 | 0.2 | 5.06 |
| 3 | 0.5 | 5.33 |
| 4 | 1.0 | 5.60 |
| 5 | 2.0 | 5.87 |
| 6 | 4.0 | 6.09 |
| 7 | 6.0 | 6.35 |
| 8 | 10.0 | 6.74 |
| 9 | 20.0 | 7.05 |
| 10 | 32.0 | 7.25 |

The P to S velocity ratio is 1.70.

by uncertainties in the velocity model (for details, see Bouchaala et al., 2013).

### 2.2. Calculation of focal mechanisms

The focal mechanisms of the whole dataset of 463 micro-earthquakes were calculated through the inversion of P-wave amplitudes. During pre-processing, the velocity records were numerically integrated into displacement records and subsequently band-pass filtered in the frequency range of 1–35 Hz in order to suppress high- and low-frequency seismic noise. A very low-frequency signal (less than 1 Hz) was removed, because it was distorted by the sensors used, and a very high-frequency signal (higher than 35 Hz) was suppressed, because it was quite sensitive to small-scale inhomogeneities not considered in the velocity model. The amplitudes were corrected for amplification factors obtained by the network calibration procedure proposed by Davi and Vavryčuk (2012). The first maximum amplitudes of the direct P waves were measured by an analyst and inverted for full moment tensors. Green's functions were computed using the ray method (Červený, 2001) in a layered velocity model defined in Table 1 and further smoothed to a gradient model for a better performance of the ray-tracing procedure. The Green's functions take into account the effects of the flat free Earth's surface. The full moment tensors (MT) were obtained using the generalized linear inversion and decomposed into double-couple (DC), isotropic (ISO) and compensated linear vector dipole (CLVD) components (Vavryčuk, 2002, 2011b). The reliability of the MT was roughly assessed by computing the root-mean-square residuals (RMS) between the synthetic and observed amplitudes. Based on the RMS, we selected 250 micro-earthquakes with the most accurate focal mechanisms. The accuracy of the moment tensors can be quantified using several alternative approaches (Fojtíková et al., 2010; Hardebeck and Shearer, 2002; Šílený, 2009; Vavryčuk et al., 2008). Here, the accuracy was quantified by repeating the inversions of randomly generated noisy amplitudes with a maximum noise level of 20%, using mislocated hypocenters with an error of 250 m in the epicenter and of 500 m in depth, and using slightly different velocity models with velocity perturbations of 5% from the original model. From these tests we were able to estimate the standard errors in the strike, dip and rake angles which should be less than 3°.

### 2.3. Results

The epicenters and the focal mechanisms of the selected 250 micro-earthquakes are shown in Fig. 2. The epicenters form a cluster roughly elongated in the NS direction which coincides with the orientation of the main active fault with a strike of 169°. The focal mechanisms display three different types: two of them are left-lateral strike slips, the first one with a weak normal component (in red), the second one with a weak reverse component (in black); and the third mechanism is the right-lateral strike slip with a normal component (in blue). The epicenters of the micro-earthquakes, whose focal mechanisms are denoted in red, are scattered over the whole focal area. Therefore, this mechanism can be considered as prevailing and characteristic for the main active fault. The epicenters of the micro-earthquakes displaying the other focal mechanisms form only small patches in the focal area. These patches are clearly visible in the depth sections (see Fig. 3): cross and in-plane sections with respect to

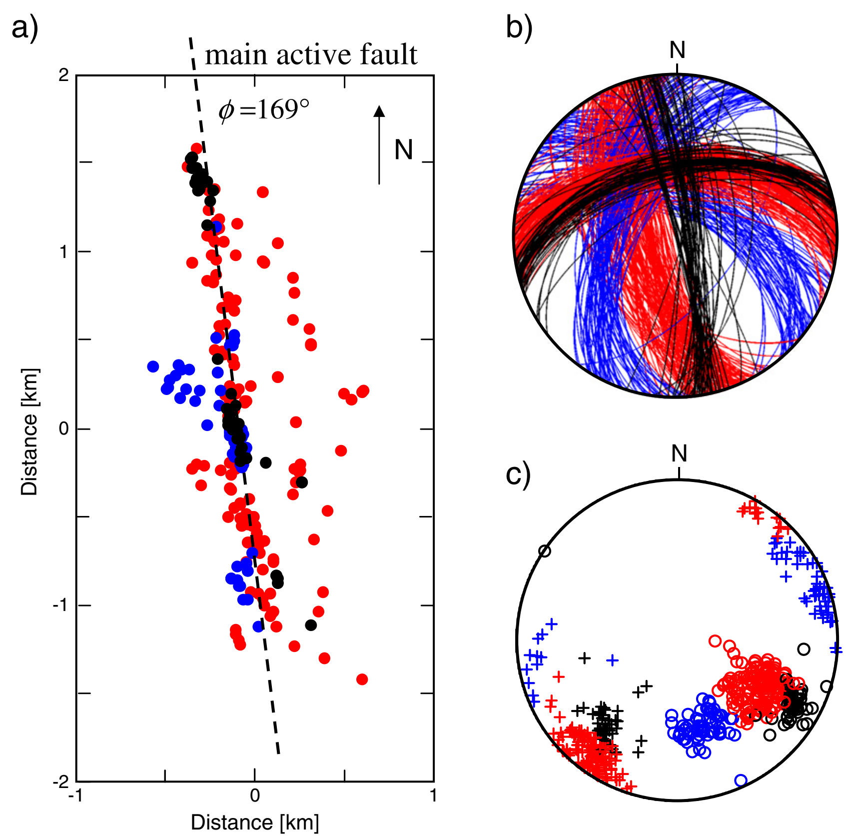


**Fig. 2.** (a) A map view with relocated epicenters, (b) nodal lines and (c) the P/T axes of the focal mechanisms of the 250 selected micro-earthquakes. The dashed line in (a) shows the orientation of the main active fault in the area. The P and T axes are denoted by open circles and plus signs, respectively. The epicenters, the nodal lines and the P/T axes are color-coded according to the type of focal mechanism: (1) the left-lateral strike slip with mean values $\varphi=169°$, $\delta=74°$, and $\lambda=-44°$ (in red), (2) the left-lateral strike slip with mean values $\varphi=359°$, $\delta=85°$, and $\lambda=32°$ (in black), and (3) the right lateral strike slip with mean values $\varphi=304°$, $\delta=66°$, and $\lambda=-137°$ (in blue). The lower-hemisphere equal-area projection is used in (b) and (c).

the main fault. In particular, the cross-section indicates the existence of several differently oriented small-scale fault segments.

Fig. 3 shows the proposed segmentation of the fault area. Fault segment 1 forms the shallow part of the fault at depths between 7 and 8 km. The fault continues down to depth as fault segment 2, which is slightly steeper and spans depths from 8 to 11 km. The focal mechanisms of events in segments 1 and 2 are similar in strike, but they differ slightly in the dip angle (both mechanisms are marked in red). Segment 2 of the fault is further crossed by three other fault segments: 3, 4 and 5. Fault segment 3 strikes N-S similarly as segments 1 and 2, but this fault segment is reverse. Fault segments 4 and 5 form an echelon with a strike of 304°. The orientations of the fault segments were determined using two independent methods: (1) from the least-squares fitting of visually selected foci of events by a plane (see Fig. 3), and (2) from the fault plane solutions of these events (see Fig. 4). The classification of foci according to their focal mechanism also reveals some other small patches (Fig. 3, in-plane section) with the focal mechanisms different from the prevailing focal mechanism (clusters of black or blue dots with no assigned number). Since the number of events was small for them, we could not calculate the orientation of these segments by least-squares fitting the foci.

## 3. Stress conditions on faults

### 3.1. Definition of fault instability

In order to understand, why differently oriented fault segments were activated during the swarm activity, the traction on the individual fault segments generated by tectonic stress has to be analyzed. According to the Mohr–Coulomb failure criterion (Beeler et al., 2000; Scholz, 2002; Zoback, 2007), shear traction on an active fault must exceed the critical value $\tau_c$, calculated from cohesion $C$, fault friction $\mu$, and effective normal traction $\sigma$:

$$\tau_c = C + \mu\sigma \quad (1)$$

or equivalently

$$\tau_c = C + \mu(\sigma_n - p) \quad (2)$$

where $\sigma_n$ is the normal traction and $p$ is the pore pressure. If the Mohr–Coulomb failure criterion is satisfied, the fault becomes unstable and an earthquake occurs along this fault. The higher the shear traction difference, $\Delta\tau = \tau - \tau_c$, the higher the instability of the

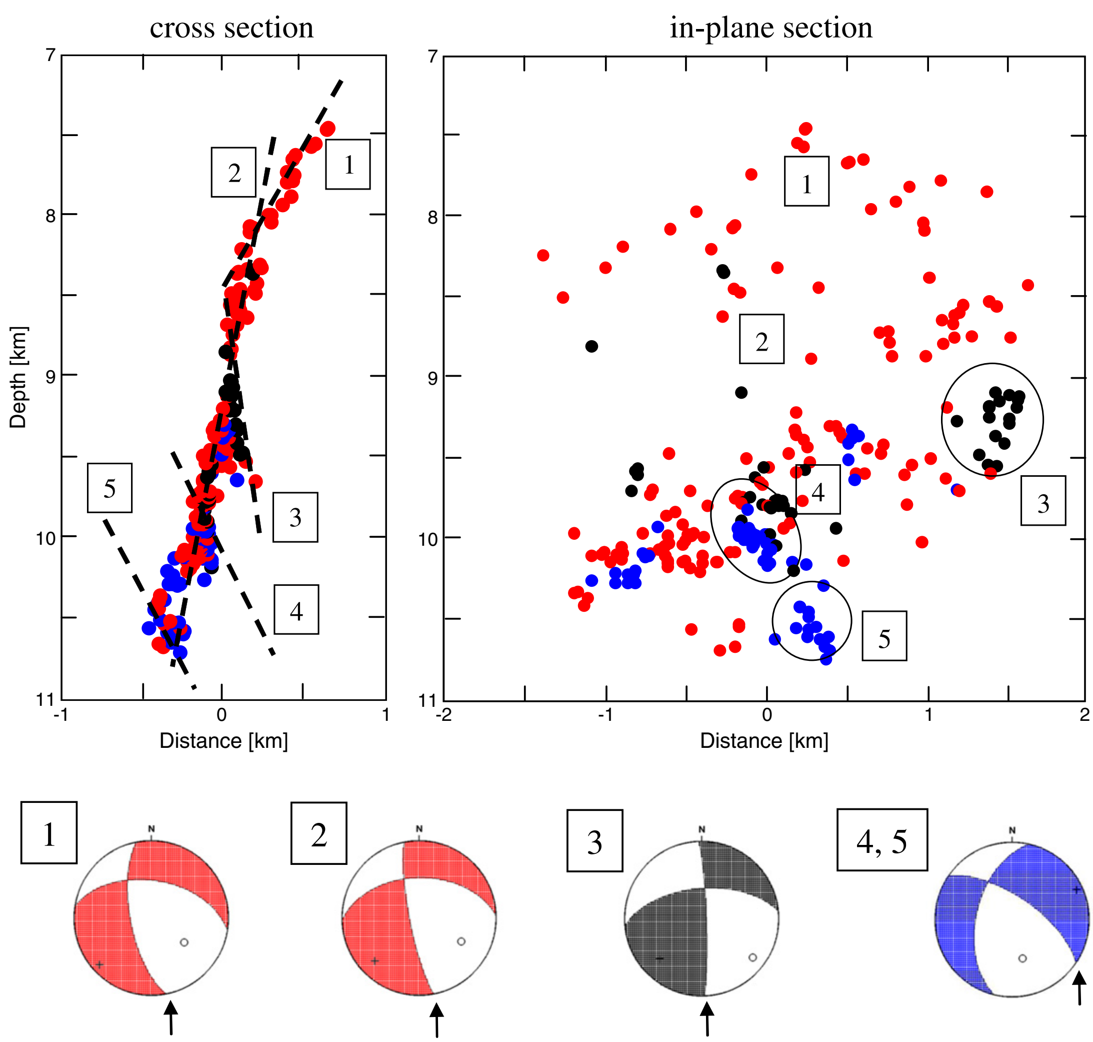


**Fig. 3.** The segmentation of the focal area using plane fitting to foci and the diversity of focal mechanisms. Upper plots show the depth sections of the main active fault, the lower plots show the basic types of the focal mechanisms. The numbers identify the individual fault segments. The arrows in the focal mechanism plots indicate the fault planes. The focal mechanisms in the lower plots (from left to right) are characterized by the following strike, dip and rake angles: (1) $\varphi = 169°$, $\delta = 68°$, and $\lambda = -44°$ (in red), (2) $\varphi = 169°$, $\delta = 80°$, and $\lambda = -44°$ (in red), (3) $\varphi = 359°$, $\delta = 85°$, and $\lambda = 32°$ (in black), and (4, 5) $\varphi = 304°$, $\delta = 66°$, and $\lambda = -137°$ (in blue).

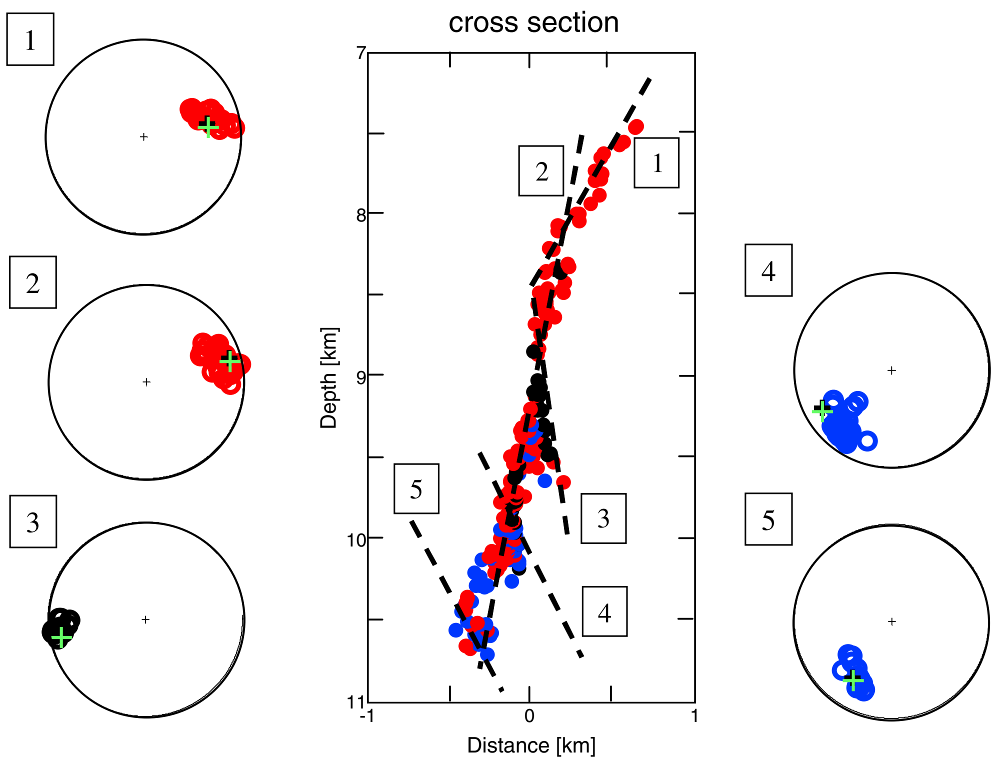


**Fig. 4.** The orientations of the fault segments determined from plane fitting to foci and from focal mechanisms. The numbers identify the individual fault segments. The open circles in the focal spheres show the orientations of the fault normals computed from the focal mechanisms of events belonging to the individual fault segments. The green plus signs mark the fault normals computed using the fitting of plane to foci.

fault and the higher the susceptibility of the fault to be activated. Obviously, a prominent fault is the one that is optimally oriented in the present stress field. According to Vavryčuk (2011a), this fault is called the principal fault, defined as the most unstable and most susceptible fault to failure (see Fig. 5). If we scale the instability value to 0 for the fault with the most stable fault orientation (the fault with the normal parallel to maximum compression $\sigma_1$) and to 1 for the most unstable fault orientation (the principal fault), we can measure the fault instability $I$ of all fault orientations in the range from 0 to 1 (see Fig. 5) using the following formula:

$$I = \frac{\tau - \mu(\sigma - \sigma_1)}{\tau_c - \mu(\sigma_c - \sigma_1)} \quad (3)$$

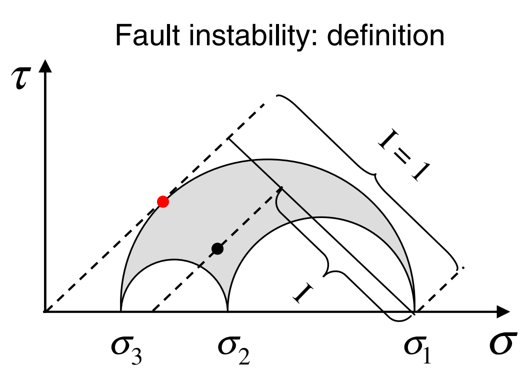


**Fig. 5.** The definition of the fault instability in the Mohr's diagram. The red dot marks the tractions of the principal fault (i.e. the most unstable fault in the stress field, see Vavryčuk, 2011a) characterized by instability $I = 1$. The black dot marks the tractions of an arbitrarily oriented fault with instability $I$. Quantities $\tau$ and $\sigma$ are the shear and the effective normal tractions, respectively; $\sigma_1$, $\sigma_2$ and $\sigma_3$ are the effective principal stresses.

where $\tau_c$ and $\sigma_c$ are the shear traction and effective normal traction along the principal fault (Fig. 5, red dot), and $\tau$ and $\sigma$ are the shear traction and effective normal traction along the analyzed fault (Fig. 5, black dot).

Since Eq. (3) is independent of absolute stress values, the fault instability $I$ can be evaluated just from friction $\mu$, shape ratio $R$, $R = (\sigma_1 - \sigma_2)/(\sigma_1 - \sigma_3)$, and from directional cosines $\mathbf{n}$ defining the inclination of the fault plane from the principal stress axes. If we scale the reduced stress tensor as follows:

$$\sigma_1 = -1, \sigma_2 = 2R - 1, \sigma_3 = 1 \quad (4)$$

we get

$$\tau_c = \frac{1}{\sqrt{1+\mu^2}}, \sigma_c = \frac{\mu}{\sqrt{1+\mu^2}} \quad (5)$$

and consequently

$$I = \frac{\tau + \mu(\sigma + 1)}{\mu + \sqrt{1+\mu^2}} \quad (6)$$

where $\mu$ is positive and

$$\sigma = -n_1^2 + (2R-1)n_2^2 + n_3^2,$$
$$\tau = \sqrt{n_1^2 + (2R-1)^2 n_2^2 + n_3^2 - \left(-n_1^2 + (2R-1)n_2^2 + n_3^2\right)^2}. \quad (7)$$

Note that the fault instability has been studied so far using the so-called slip tendency (Morris et al., 1996), normalized slip tendency (Lisle and Srivastava, 2004), fault reactivation risk/potential (Mildren et al., 2002; van Ruth et al., 2006) and the normalized fault reactivation potential (Švancara et al., 2008). The fault instability defined in Eqs. (3) and (6) yields similar values as the normalized fault reactivation potential introduced by Švancara et al. (2008). However, the fault instability is introduced in a more comprehensible way and expressed in a simple explicit form.

### 3.2. Instability of faults in the West Bohemia region

Fig. 6a shows the fault instability on the focal sphere for tectonic stress in the West Bohemia region. The tectonic stress was calculated from very accurate focal mechanisms of the 99 selected micro-earthquakes of the 2008 swarm (Vavryčuk, 2011a). The micro-earthquakes have been selected to ensure a variety of focal mechanisms and a balanced representation of mechanisms associated with the two conjugate active fault systems in the area. The Angelier (2002) stress inversion yielded the $\sigma_1$, $\sigma_2$ and $\sigma_3$ principal stress directions (azimuth/plunge): 146°/48°, 327°/42° and 237°/1°. The optimum shape ratio $R$ determined from the distribution of the P and T axes on the focal sphere was 0.80 (Vavryčuk, 2011a). Fig. 6a indicates that the most stable fault planes have their normals close to $\sigma_1$ ($I=0$) or $\sigma_2$ ($I=0.5$). The most unstable fault planes with $I=1$ have their normals in directions between $\sigma_1$ and $\sigma_3$ being inclined from $\sigma_3$ by about 32° for a fault friction of 0.5.

Fig. 6b shows the positions of active fault planes on the focal sphere determined from the focal mechanisms of the 250 selected micro-earthquakes. The figure indicates that the focal mechanisms of types 1 and 2 (in red) and 4 and 5 (in blue) are associated with highly unstable fault planes ($I>0.9$). The focal mechanisms of type 3 (in black) are less unstable ($0.9>I>0.7$). The unfavorable orientation of the type 3 focal mechanisms with respect to stress is also visible in Mohr's diagrams (Fig. 7). The shear traction is remarkably lower than for the other types of focal mechanisms. Also the effective normal traction is small and might occasionally become extensive, which would result in tensile opening. This indicates that the micro-earthquakes occurring on fault segment 3 are probably shear-tensile events as described by Vavryčuk (2001, 2011b) and by Fischer and Guest (2011).

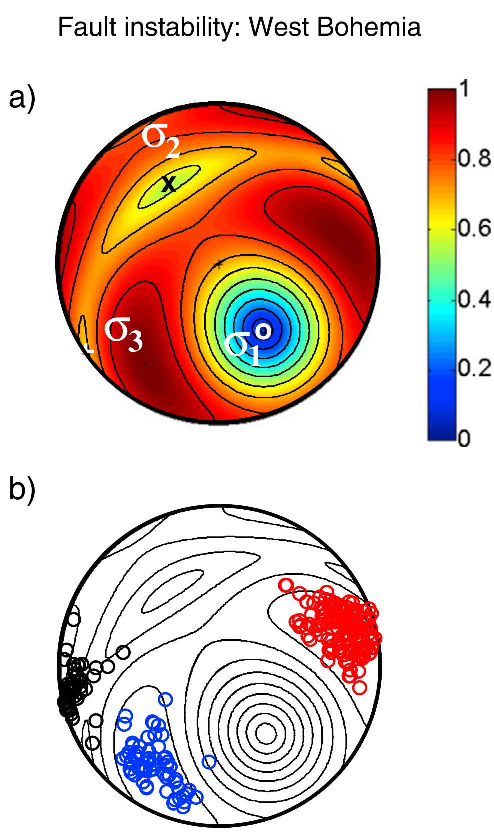


**Fig. 6.** (a) The distribution of the fault instability on the focal sphere for the stress field in the West Bohemia region. The fault instability is shown for all possible fault normals; it is color-scaled and ranges between 0 (the most stable plane) and 1 (the most unstable plane). The lower-hemisphere equal-area projection. (b) The isolines of the fault instability and the distribution of fault normals on the focal sphere calculated from focal mechanisms of the 250 analyzed events. The fault normals are color-coded according to their focal mechanisms. The directions of the $\sigma_1$, $\sigma_2$ and $\sigma_3$ axes are (azimuth/plunge): 146°/48°, 327°/42° and 237°/1°. The shape ratio $R$ is 0.80 and the fault friction $\mu$ is 0.5 (Vavryčuk, 2011a).

## 4. Discussion and conclusions

Although the focal zone of the 2008 swarm in West Bohemia is very small with a length of less than 4 km, its structure is complex. It comprises several fault segments differently orientated, mutually intersecting and activated at different times (Fig. 8). The orientation of the fault segments was found independently by foci clustering and by the focal mechanisms. The fault segments were analyzed according to their instability which was calculated from the Mohr–Coulomb failure criterion. The fault instability value ranges from 0 for the most stable fault orientation (with the fault normal parallel to $\sigma_1$) to 1 for the most unstable fault orientation (principal fault). The majority of the fault segments are characterized by high instability ($I>0.9$) having an orientation close to the principal faults. These fault segments are optimally oriented for a shear failure with respect to the tectonic stress in the area. However, some of earthquakes occurred on slightly misoriented fault segments characterized by significantly lower shear traction. The unfavorable orientation of focal mechanisms with respect to stress is also visible in the Mohr's circle diagram. These earthquakes are probably more

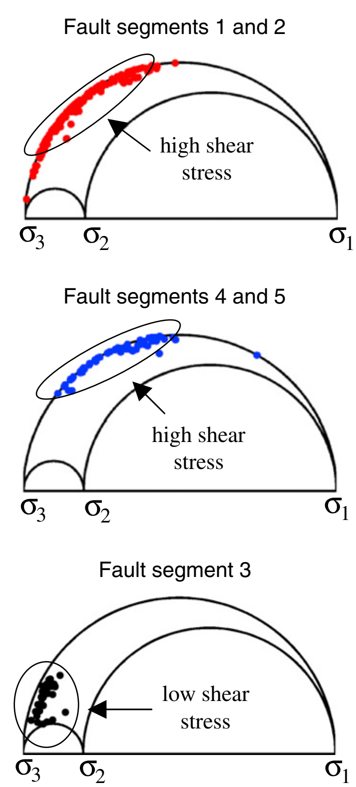


**Fig. 7.** Fault planes (full dots) in the Mohr's diagrams for three different types of focal mechanisms. The fault planes calculated from focal mechanisms are color-coded: the red dots correspond to foci on fault segments 1 and 2; the blue dots correspond to foci on fault segments 4 and 5; and the black dots correspond to foci on fault segment 3. Fault segments 1,2, 4 and 5 are optimally oriented, segment 3 is misoriented with respect to stress.

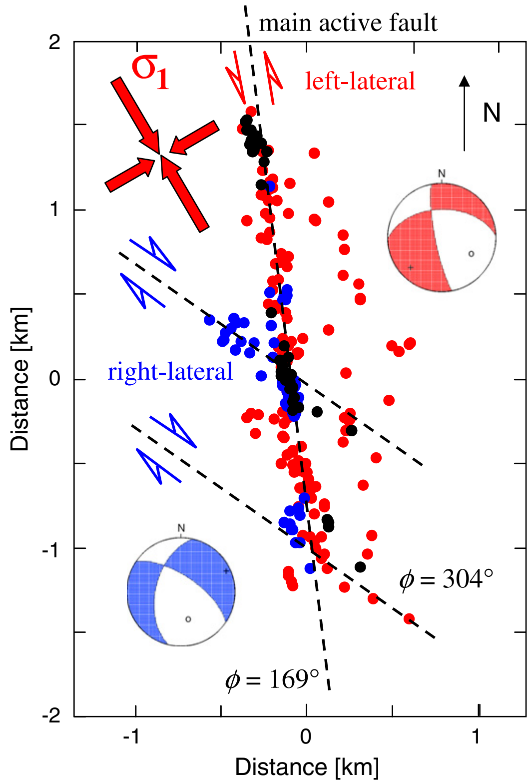


**Fig. 8.** Tectonic sketch of the focal zone with color-coded epicenters according to their focal mechanisms. The dashed lines show the active principal fault segments. The full red arrows show the orientation of the maximum and minimum compressive stress axes. The beach balls show the focal mechanisms associated with the principal faults: the left-lateral (in red) and the right-lateral (in blue) strike slips.

tensile and activated by a local redistribution of Coulomb stress during the swarm activity.

## Acknowledgments

We thank Marco Bohnhoff and Jiří Zahradník for helpful reviews, Josef Havíř and Pavla Hrubcová for fruitful discussions, Alena Boušková, Josef Horálek and Jan Michálek for providing us with the data from the 2008 swarm activity in West Bohemia and for their kind help with the data pre-processing. The work was supported by the Grant Agency of the Czech Republic, grant no. P210/12/1491, by the European Community's FP7 Consortium Project AIM “Advanced Industrial Microseismic Monitoring”, grant agreement no. 230669, and by the Project CzechGeo, grant no. LM2010008.

## References

Angelier, J., 2002. Inversion of earthquake focal mechanisms to obtain the seismotectonic stress IV — a new method free of choice among nodal lines. Geophysical Journal International 150, 568–609.
Babuška, V., Plomerová, J., Fischer, T., 2007. Intraplate seismicity in the western Bohemian Massif (central Europe): a possible correlation with a paleoplate junction. Journal of Geodynamics 44, 149–159.
Bankwitz, P., Schneider, G., Kämpf, H., Bankwitz, E., 2003. Structural characteristics of epicentral areas in Central Europe: study case Cheb Basin (Czech Republic). Journal of Geodynamics 35, 5–32.
Beeler, N.M., Simpson, R.W., Hickman, S.H., Lockner, D.A., 2000. Pore fluid pressure, apparent friction, and Coulomb failure. Journal of Geophysical Research 105, 25.533–25.542.
Bouchaala, F., Vavryčuk, V., Fischer, T., 2013. Accuracy of the master-event and double-difference locations: synthetic tests and applicationto seismicity inWest Bohemia, Czech Republic. Journal of Seismology. http://dx.doi.org/10.1007/s10950-013-9357-4.
Červený, V., 2001. Seismic Ray Theory. Cambridge Univ. Press, Cambridge.
Davi, R., Vavryčuk, V., 2012. Seismic network calibration for retrieving accurate moment tensors. Bulletin of the Seismological Society of America 102, 2491–2506. http://dx.doi.org/10.1785/0120110344.
Fischer, T., Guest, A., 2011. Shear and tensile earthquakes caused by fluid injection. Geophysical Research Letters 38, L05307. http://dx.doi.org/10.1029/2010GL045447.
Fischer, T., Horálek, J., 2003. Space-time distribution of earthquake swarms in the principal focal zone of the NW Bohemia/Vogtland seismoactive region: period 1985–2001. Journal of Geodynamics 35, 125–144.
Fischer, T., Horálek, J., Michálek, J., Boušková, A., 2010. The 2008 West Bohemia earthquake swarm in the light of the WEBNET network. Journal of Seismology 14, 665–682.
Fojtíková, L., Vavryčuk, V., Cipciar, A., Madarás, J., 2010. Focal mechanisms of micro-earthquakes in the Dobrá Voda seismoactive area in the Malé Karpaty Mts. (Little Carpathians), Slovakia. Tectonophysics 492, 213–229. http://dx.doi.org/10.1016/j.tecto.2010.06.007.
Hardebeck, J.L., Shearer, P.M., 2002. A new method for determining first-motion focal mechanisms. Bulletin of the Seismological Society of America 92, 2264–2276.
Heidbach, O., Tingay, M., Barth, A., Reinecker, J., Kurfeß, D., Müller, B., 2008. The World Stress Map database release 2008. http://dx.doi.org/10.1594/GFZ.WSM.Rel2008 (last accessed February 2012).
Hermann, R.B., 1979. FASTHYPO — a hypocenter location program. Earthquake Notes 50, 25–37.
Lisle, R.J., Srivastava, D.C., 2004. Test of the frictional reactivation theory for faults and validity of fault-slip analysis. Geology 32, 569–572.
Málek, J., Janský, J., Horálek, J., 2000. Layered velocity models of the western Bohemia region. Studia Geophysica et Geodaetica 44, 475–490.
Mildren, S.D., Hillis, R.R., Kaldi, J., 2002. Calibrating predictions of fault seal reactivation in the Timor Sea. Australian Petroleum Production & Exploration Association Journal 42, 187–202.
Morris, A., Ferrill, D.A., Henderson, D.B., 1996. Slip-tendency analysis and fault reactivation. Geology 24, 275–278.
Scholz, C.H., 2002. The Mechanics of Earthquakes and Faulting. Cambridge Univ. Press, Cambridge.
Šílený, J., 2009. Resolution of non-double-couple mechanisms: simulation of hypocentre mislocation and velocity structure mismodelling. Bulletin of the Seismological Society of America 99, 2265–2272.
Švancara, J., Havíř, J., Conrad, W., 2008. Derived gravity field of the seismogenic upper crust of SE Germany and West Bohemia and its comparison with seismicity. Studia Geophysica et Geodaetica 52, 567–588.
van Ruth, P.J., Nelson, E.J., Hillis, R.R., 2006. Fault reactivation potential during CO2 injection in the Gippsland Basin, Australia. Exploration Geophysics 37, 50–59.
Vavryčuk, V., 2001. Inversion for parameters of tensile earthquakes. Journal of Geophysical Research 106 (B8), 16.339–16.355. http://dx.doi.org/10.1029/2001JB000372.
Vavryčuk, V., 2002. Non-double-couple earthquakes of January 1997 in West Bohemia, Czech Republic: Evidence of tensile faulting. Geophysical Journal International 149, 364–373. http://dx.doi.org/10.1046/j.1365-246X.2002.01654.x.
Vavryčuk, V., 2011a. Principal earthquakes: theory and observations for the 2008 West Bohemia swarm. Earth and Planetary Science Letters 305, 290–296. http://dx.doi.org/10.1016/j.epsl.2011.03.002.
Vavryčuk, V., 2011b. Tensile earthquakes: theory, modeling, and inversion. Journal of Geophysical Research 116, B12320. http://dx.doi.org/10.1029/2011JB008770.
Vavryčuk, V., Bohnhoff, M., Jechumtálová, Z., Kolář, P., Šílený, J., 2008. Non-double-couple mechanisms of micro-earthquakes induced during the 2000 injection experiment at the KTB site, Germany: a result of tensile faulting or anisotropy of a rock? Tectonophysics 456, 74–93. http://dx.doi.org/10.1016/j.tecto.2007.08.019.
Waldhauser, F., Ellsworth, W.L., 2000. A double-difference location algorithm: method and application to the Northern Hayward Fault, California. Bulletin of the Seismological Society of America 78, 1353–1368.
Zoback, M.D., 2007. Reservoir Geomechanics. Cambridge Univ. Press, Cambridge.